


# Ultrasmall Au clusters supported on pristine and defected CeO<sub>2</sub>: Structure and stability

Cite as: J. Chem. Phys. **151**, 174702 (2019); <https://doi.org/10.1063/1.5126187>

Submitted: 31 August 2019 . Accepted: 14 October 2019 . Published Online: 04 November 2019

Si-Da Huang, Cheng Shang , and Zhi-Pan Liu 



View Online



Export Citation



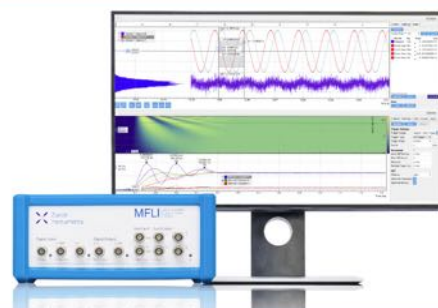
CrossMark

## Challenge us.

What are your needs for periodic  
signal detection?



Zurich  
Instruments



# Ultrasmall Au clusters supported on pristine and defected CeO<sub>2</sub>: Structure and stability

Cite as: J. Chem. Phys. 151, 174702 (2019); doi: 10.1063/1.5126187

Submitted: 31 August 2019 • Accepted: 14 October 2019 •

Published Online: 4 November 2019



View Online



Export Citation



CrossMark

Si-Da Huang, Cheng Shang,<sup>a)</sup>  and Zhi-Pan Liu<sup>a)</sup> 

## AFFILIATIONS

Collaborative Innovation Center of Chemistry for Energy Material, Shanghai Key Laboratory of Molecular Catalysis and Innovative Materials, Key Laboratory of Computational Physical Science (Ministry of Education), Department of Chemistry, Fudan University, Shanghai 200433, China

**Note:** The paper is part of the JCP Special Topic Collection on Catalytic Properties of Model Supported Nanoparticles.

<sup>a)</sup>Electronic addresses: [cshang@fudan.edu.cn](mailto:cshang@fudan.edu.cn) and [zpliu@fudan.edu.cn](mailto:zpliu@fudan.edu.cn)

## ABSTRACT

The atomistic simulation of supported metal catalysts has long been challenging due to the increased complexity of dual components. In order to determine the metal/support interface, efficient theoretical tools to map out the potential energy surface (PES) are generally required. This work represents the first attempt to apply the recently developed SSW-NN method, stochastic surface walking (SSW) global optimization based on global neural network potential (G-NN), to explore the PES of a highly controversial supported metal catalyst, Au/CeO<sub>2</sub>, system. By establishing the ternary Au–Ce–O G-NN potential based on first principles global dataset, we have searched for the global minima for a series of Au/CeO<sub>2</sub> systems. The segregation and diffusion pathway for Au clusters on CeO<sub>2</sub>(111) are then explored by using enhanced molecular dynamics. Our results show that the ultrasmall cationic Au clusters, e.g., Au<sub>4</sub>O<sub>2</sub>, attaching to surface structural defects are the only stable structural pattern and the other clusters on different CeO<sub>2</sub> surfaces all have a strong energy preference to grow into a bulky Au metal. Despite the thermodynamics tendency of sintering, Au clusters on CeO<sub>2</sub> have a high kinetics barrier (>1.4 eV) in segregation and diffusion. The high thermodynamics stability of ultrasmall cationic Au clusters and the high kinetics stability for Au clusters on CeO<sub>2</sub> are thus the origin for the high activity of Au/CeO<sub>2</sub> catalysts in a range of low temperature catalytic reactions. We demonstrate that the global PES exploration is critical for understanding the morphology and kinetics of metal clusters on oxide support, which now can be realized via the SSW-NN method.

Published under license by AIP Publishing. <https://doi.org/10.1063/1.5126187>

## I. INTRODUCTION

The past two decades have witnessed tremendous research interest on Au-based catalysts that may exhibit outstanding low temperature catalytic ability<sup>1,2</sup> for a wide range of reactions, e.g., CO oxidation by atmospheric air,<sup>3,4</sup> methanol synthesis,<sup>5</sup> NO reduction,<sup>6,7</sup> hydrogenation of ethene,<sup>8</sup> and so on. Both the nature of Au<sup>9</sup> (oxidation state and particle size) and the type of oxide supports<sup>10–12</sup> (reducible and irreducible) are found to be critical for the activity. Among the catalysts, the ceria supported gold (Au/CeO<sub>2</sub>) appears to be exceptional: it can catalyze water-gas-shift (WGS) reactions starting from ~350 K to produce high-grade hydrogen and has a high stability.<sup>13,14</sup> Since CeO<sub>2</sub> is long known to be a reducible oxide, similar to TiO<sub>2</sub>, with a good oxygen storage

ability,<sup>15</sup> it was long assumed that the oxygen vacancies on the support play key roles in the Au/CeO<sub>2</sub> system.<sup>16</sup> However, the seminal work by Fu *et al.* suggested that oxidized gold (e.g., Au<sup>+</sup> or Au<sup>3+</sup>) is the active site for the WGS reaction.<sup>13</sup> The origin for the high catalytic activity of Au/CeO<sub>2</sub> has been a subject of debate ever since.

In the first experiment by Fu *et al.*, the catalytic activity has been measured before and after cyanide leaching for the Au/CeO<sub>2</sub> (La-doped) catalyst, which is used to remove large metallic Au particles on support.<sup>13</sup> The nearly identical catalytic performance after cyanide leaching is thus a proof that small cationic Au particles or even single Au cations should be responsible for the activity. Later experiments by Guzman *et al.* support this conclusion by showing a direct correlation between the CO oxidation rate

with the concentration of Au cations, which can be measured by IR spectroscopy of the Au–CO bond.<sup>17</sup> By using *in situ* extended X-ray absorption fine structure (EXAFS), Tibiletti *et al.*<sup>18</sup> observed the Au–Ce short contact,  $\sim 3.35$  Å, in the fresh Au/CeO<sub>2</sub> catalysts, which are assigned to the finely dispersed cationic Au on CeO<sub>2</sub>. In contrast, Kim *et al.* conducted leaching experiments similar to those conducted by Fu *et al.* for the Au/CeO<sub>2</sub> catalyst but observed that the CO consumption rate in the WGS reaction is significantly lower after leaching and thus suggested that nanocrystalline Au, presumably Au<sup>0</sup>, are also important reactive sites for the WGS reaction.<sup>19</sup> In fact, the Au cations are found to be unstable under the WGS reaction condition and can convert to metallic Au as evident from *in situ* time-resolved X-ray spectra [EXAFS and x-ray absorption near-edge structure (XANES)].<sup>18,20</sup> Recently, surface science studies by using STM, however, seem to support the earliest speculation that there are ample O (subsurface) defects on the CeO<sub>2</sub> thin film.<sup>21</sup> The supported Au atoms on these O vacancy sites are expected to be negatively charged, which is indeed confirmed from theory.<sup>22</sup> Obviously, the puzzles on the morphology and oxidation state of Au on CeO<sub>2</sub> remain unsettled, which is partly due to the fact that metallic nanoparticles are present dominantly in real catalysts, and thus, the pursuit for the origin of ultra-small cationic Au becomes extremely difficult. The key questions, such as where cationic Au grow and how stable they are, are not answered yet.

Although first principles calculations are now standard tools for understanding surface reactions, the simulation of supported metal catalysts, Au/CeO<sub>2</sub> in particular, has been facing two challenges: (i) the large size of the metal/support system and (ii) the high computational cost using standard density functionals (e.g., convergence difficulty in electronic structure) for *f*-block element Ce due to the spin polarization and localization when Ce<sup>4+</sup> is reduced to Ce<sup>3+</sup>.<sup>23,24</sup> The computation of Au (particles) on CeO<sub>2</sub> would easily involve hundreds of atoms to include the ceria support, not even mentioning the exploration for the global potential energy surface (PES) and the diffusion kinetics of supported Au clusters. Nevertheless, by using relatively small unit cells, previous theoretical attempts by many groups (e.g., Liu *et al.*,<sup>25</sup> Zhang *et al.*,<sup>26</sup> and Camellone and Fabris<sup>27</sup>) indicated that the Au atom adsorbs on the top of surface O and is positively charged by transferring one electron from Au to underneath Ce (thus, Ce<sup>4+</sup> to Ce<sup>3+</sup>), which suggests a strong interaction between Au and CeO<sub>2</sub> support. As for the catalytic activity, small Au clusters are found enough to catalyze WGS and CO oxidation.<sup>25,28–30</sup> Theory thus suggests that the stability of ultra-small Au clusters under reaction conditions should be the key to the activity of the Au/CeO<sub>2</sub> system. It is of significance to search for the most stable ultra-small Au clusters, which could turn out to be the key active site in catalytic reactions.

In this work, we aim to explore the configurations of ultra-small Au clusters on CeO<sub>2</sub> and determine their thermodynamics and kinetics stability. By using stochastic surface walking (SSW) global optimization<sup>31,32</sup> based on global neural network potential (G-NN),<sup>33,34</sup> i.e., the SSW-NN method,<sup>35,36</sup> and enhanced molecular dynamics (MD),<sup>37,38</sup> we reveal the global minimum structure for Au clusters on different CeO<sub>2</sub> surfaces together with the segregation/diffusion pathways for Au clusters on the pristine CeO<sub>2</sub> surface. Our results provide important new insights into the chemistry of Au/CeO<sub>2</sub> catalysis.

## II. METHODOLOGY AND CALCULATION SETUPS

All simulations based on neural network potential were carried out by using our recently developed LASP software,<sup>39</sup> the large-scale atomic simulation with neural network potential ([www.lasphub.com](http://www.lasphub.com)) that implements the data-generation, training, and evaluation of the global neural network (G-NN) potential.<sup>33</sup> In addition to G-NN functionalities, LASP provides various interfaces to common first principles density functional theory (DFT) packages as well as multiple modules for PES exploration. In this section, we will review briefly the procedure to construct a global NN potential for the Au–Ce–O ternary system and describe our implementation of enhanced MD simulation with bias potentials using power-type structural descriptors (PTSDs).<sup>34</sup>

### A. Global neural network potential for Au/CeO<sub>2</sub>

The ternary Au–Ce–O G-NN potential is obtained by self-learning of the SSW global PES dataset that covers a wide range of Au<sub>x</sub>CeO<sub>y</sub> compositions with different structural types (bulks, surfaces, and clusters). The dataset is calculated by high-accuracy DFT calculations as implemented in VASP.<sup>40</sup> The G-NN training is achieved by minimizing the difference between NN and DFT results on the total energy, forces, and stresses. The typical procedure and the hyperparameters utilized can be found in our recent publications.<sup>39,41</sup>

In total, more than 10<sup>7</sup> structures on Au<sub>x</sub>CeO<sub>y</sub> PES are visited by SSW-NN during NN potential generation, and the final training dataset of Au<sub>x</sub>CeO<sub>y</sub> consists of 33 654 structures that are selected to represent the global PES. The details of the dataset are listed in Table S1 of the [supplementary material](#), which covers metallic Au, oxides CeO<sub>x</sub> and AuO<sub>x</sub>, and supported Au/CeO<sub>x</sub> systems. To build the NN potential, each elementary network (Au, Ce, and O) contains 186 input neurons from different types of PTSDs, associated with three hidden layers (60-50-50) (see Sec. 1 of the [supplementary material](#) for more details). In total,  $\sim 51$  000 network parameters are utilized to train the AuCeO system. For the final G-NN potential, the root-mean-square (rms) errors for the energy and the force are 6.115 meV per atom and 0.152 eV/Å, respectively. We have benchmarked the NN calculations against DFT results for the target Au/CeO<sub>2</sub> systems, which shows that the energy rms error is below 1 meV per atom (see Table S2 of the [supplementary material](#)). This small error suggests that the NN PES is a good approximation to DFT PES of Au<sub>x</sub>CeO<sub>y</sub> and can be utilized to expedite the global structure search and pathway determination. Due to the large size of the supported metal/oxide system, we report all results from G-NN calculations.

For the G-NN training dataset generation, the plane-wave DFT calculations as implemented in VASP (Vienna *ab initio* simulation package) were utilized to evaluate the energy and forces, where the DFT functional is at the level of the generalized gradient approximation with the Perdew–Burke–Ernzerhof functional (PBE)<sup>42</sup> with the Hubbard term correction<sup>43,44</sup> for on-site Coulomb interaction (PBE + U, U = 5.0 eV for Ce 4*f* states) as typically utilized in recent literature.<sup>45–54</sup> This U value has been shown to yield the correct *f*-electron localization in the reduced CeO<sub>2</sub> (111) surface<sup>24,47–51,54</sup> as well as to produce the lattice parameters of CeO<sub>2</sub> close to experimental results.<sup>47,52,53</sup> The kinetic energy cutoff was 450 eV, and the projector augmented wave (PAW)

pseudopotential<sup>55</sup> was utilized to describe ionic core electrons. The first Brillouin zone  $k$ -point sampling utilizes the Monkhorst–Pack scheme<sup>56</sup> with an automated mesh determined by 25 times the reciprocal lattice vectors.

## B. Enhanced MD with bias potentials on general reaction coordinate

In this work, the enhanced MD technique implemented in LASP was utilized to explore the reaction pathway for Au cluster segregation and diffusion. To facilitate the barrier crossing and thus expedite the PES exploration, the enhanced MD methods such as umbrella sampling<sup>38,57</sup> and metadynamics<sup>37</sup> impose a bias potential along the predefined reaction coordinate,  $\xi$ , that can be constructed from the Cartesian coordinates. The reaction coordinate needs to be capable to distinguish the structures along the desired reaction pathway. In LASP, we implement the general reaction coordinate by using the PTSDs<sup>34</sup> that are utilized for G-NN generation to distinguish different structures. For example, a two-body general reaction coordinate,  $S_i^1$ , has the following form, which can be utilized to distinguish the local coordination environment of atom  $i$ :

$$f_c(r_{ij}) = \begin{cases} 0.5 \times \tan h^3 \left[ 1 - \frac{r_{ij}}{r_c} \right], & \text{for } r_{ij} \leq r_c \\ 0, & \text{for } r_{ij} > r_c, \end{cases} \quad (1)$$

$$R^n(r_{ij}) = r_{ij}^n \cdot f_c(r_{ij}), \quad (2)$$

$$S_i^1 = \sum_{j \neq i} R^n(r_{ij}), \quad (3)$$

$$\xi = \frac{1}{N_{\text{atom}}} \sum_i S_i^1. \quad (4)$$

In the equations,  $r_{ij}$  is the internuclear distance between atom  $i$  and  $j$ ; the cutoff radius  $r_c$  and the power  $n$  are adjustable parameters. In this work,  $r_c$  and  $n$  are chosen to be 10 Å and 0, respectively. A natural choice to construct a reaction coordinate  $\xi$  is to average the atomic PTSD value  $S_i^1$  for the entire structure of  $N$  atoms ( $N_{\text{atom}}$ ), as shown in Eq. (4). To give concrete examples for the magnitude of the two-body  $\xi$ , the fcc Au bulk (coordination number, CN = 12) has a value of 34.68; the Au(111) surface [(1 × 1) three-layer slab with 12 atoms in total, CN = 9 for surface atom] has a value of 23.62, and a planar Au<sub>4</sub> cluster (CN = 2) has a value of 2.65.

Using the general reaction coordinate  $\xi_m$  ( $m$  labels the position of the window center), we then construct the bias potential  $W_m$  in the quadratic form as Eq. (5), which, as widely utilized in umbrella sampling, introduces a restraint in the system to enforce the MD simulation trapping in a local region defined by  $\xi_m$ ,

$$W_m(\xi) = \frac{1}{2} K (\xi - \xi_m)^2. \quad (5)$$

In Eq. (5), the harmonic constant  $K$  represents the intensity of the bias potential. By gradually adjusting  $\xi_m$ , one can, therefore, drive the reaction to occur by sampling sequentially each window defined by  $\xi_m$  at the  $m$  position.

Our MD calculations were performed on the canonical (NVT) ensemble at the constant temperature 500 K. For each window, the harmonic constant  $K$  was chosen as 30 eV, and the MD simulations run for 20 ps with 1 fs for each time step. The initial configuration

in the first window adopts the global minimum structure identified from the SSW global optimization.<sup>31,32</sup> Then, the simulation for each subsequent window utilizes the initial configuration generated from the last 10% configurations in the previous window, which yields the closest coordinate value with the current window center.

## C. Atomistic model for Au/CeO<sub>2</sub>

In our simulation, the most stable surface of CeO<sub>2</sub>, CeO<sub>2</sub>(111), is modeled by a (3 × 3) four-layer slab with a (6 × 6) periodicity per layer, containing 36 CeO<sub>2</sub> entities per layer and in total 432 atoms. The bottom two layers were kept fixed at the bulk truncated position, and the top two layers were allowed to fully relax during the SSW PES search. The surface defects are also considered by either depleting one surface O (O vacancy) or creating a structural defect (removing a O–Ce–O entity). Differently sized Au clusters are then added to CeO<sub>2</sub> surfaces to represent Au/CeO<sub>2</sub> systems. The large surface area utilized is to diminish the likely interaction between Au cluster images in periodic cells and also to reduce the interaction between surface defects. The global minimum for all the systems has been identified using the SSW global optimization technique.

## III. RESULTS AND DISCUSSIONS

### A. Au clusters on pristine and defected CeO<sub>2</sub> surface

To identify the stable configuration of ultrasmall Au clusters, we have explored different Au clusters (up to 12 atom clusters), i.e., Au <sub>$x$</sub>  ( $x = 4, 8, 12$ ), on CeO<sub>2</sub> surfaces by using SSW-NN. Three types of CeO<sub>2</sub> surfaces are considered: pristine CeO<sub>2</sub>(111) denoted as CeO<sub>2</sub>-p, CeO<sub>2</sub>(111) with a surface O vacancy (1/36 ML) denoted as CeO<sub>2</sub>-O<sub>v</sub>, and CeO<sub>2</sub>(111) with structural defects modeled by a CeO<sub>2</sub> slab missing a surface O–Ce–O entity denoted as CeO<sub>2</sub>-SD. Except for CeO<sub>2</sub>-O<sub>v</sub> where the surface is partly reduced, the other two surfaces maintain the Ce:O = 1:2 stoichiometry. The most stable configuration for these surface models is first determined from more than 10<sup>5</sup> minima visited by SSW, as shown in Fig. 1.

Compared to the pristine CeO<sub>2</sub>(111), no significant surface reconstruction occurs for CeO<sub>2</sub>-O<sub>v</sub> and CeO<sub>2</sub>-SD: the surface atoms remain largely at their lattice position. For CeO<sub>2</sub>-O<sub>v</sub>, the oxygen vacancy prefers the subsurface position, as already noted previously.<sup>49,58,59</sup> Under the assumption that there is enough bulk oxide to act as a thermodynamic reservoir,<sup>60</sup> the vacancy formation energy for O vacancy,  $E_{\text{form}}^{\text{Ov}}$ , and O–Ce–O structural defect,  $E_{\text{form}}^{\text{SD}}$ , can be calculated according to the following equations:

$$E_{\text{form}}^{\text{Ov}} = E_{\text{Ov}} - E_{\text{pristine}} - \frac{1}{2} E_{\text{O}_2}, \quad (6)$$

$$E_{\text{form}}^{\text{SD}} = E_{\text{SD}} - E_{\text{pristine}} - E_{\text{CeO}_2}, \quad (7)$$

where  $E_{\text{pristine}}$ ,  $E_{\text{Ov}}$ ,  $E_{\text{SD}}$ ,  $E_{\text{O}_2}$ , and  $E_{\text{CeO}_2}$  are the total energy of CeO<sub>2</sub>-p, CeO<sub>2</sub>-O<sub>v</sub>, CeO<sub>2</sub>-SD, a gas phase O<sub>2</sub> molecule, and the bulk CeO<sub>2</sub> unit, respectively. Consequently,  $E_{\text{form}}^{\text{Ov}}$  and  $E_{\text{form}}^{\text{SD}}$  are calculated to be +1.88 eV and +2.49 eV, respectively. Both defects should be common in CeO<sub>2</sub> catalysts. In experiment, the O vacancy of CeO<sub>2</sub> can be created at elevated temperatures or under reaction

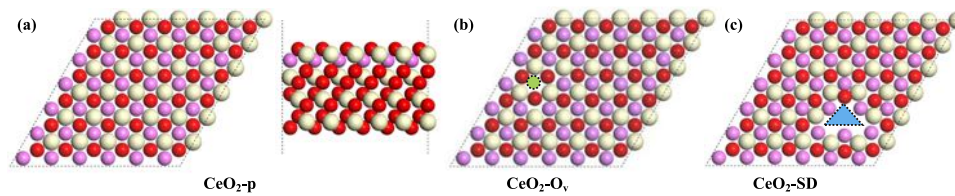


**FIG. 1.** Most stable structures for three types of  $\text{CeO}_2$  surfaces. (a)  $\text{CeO}_2\text{-p}$ : pristine  $\text{CeO}_2(111)$  surface (top and side views), (b)  $\text{CeO}_2\text{-O}_v$ : (111) surface with an oxygen vacancy (top view), and (c)  $\text{CeO}_2\text{-SD}$ : (111) surface with an O–Ce–O structural defect (top view). O atoms are in red/pink, and Ce atoms are in white. For clarity, the surface layer O and the subsurface O are in different colors, red and pink, respectively. The oxygen vacancy and missing O–Ce–O entities are indicated by dashed shapes with filled green and blue colors, respectively. Only the top  $\text{CeO}_2$  layer of the surfaces is shown in the top view.

conditions (by reacting with reductive molecules, CO and  $\text{H}_2$ ); the structural defects can be made at the catalyst preparation stage, e.g., during synthesizing nanoparticles and the subsequent high temperature calcination.

Next, extensive SSW-NN simulation has been utilized to search for the most stable structure configurations for Au clusters on  $\text{CeO}_2$  surfaces (more than  $10^5$  minima searched for each model). For each cluster with a fixed number of Au atoms, three different surfaces are considered, and thus, in total, nine systems are explored to determine the global minimum. They are  $\text{Au}_4/\text{CeO}_2\text{-p}$ ,  $\text{Au}_4/\text{CeO}_2\text{-O}_v$ ,  $\text{Au}_4\text{O}_2/\text{CeO}_2\text{-SD}$ ,  $\text{Au}_8/\text{CeO}_2\text{-p}$ ,  $\text{Au}_8/\text{CeO}_2\text{-O}_v$ ,  $\text{Au}_4\text{O}_2/\text{CeO}_2\text{-SD}$ , and  $\text{Au}_{12}/\text{CeO}_2\text{-p}$ ,  $\text{Au}_{12}/\text{CeO}_2\text{-O}_v$ ,  $\text{Au}_{12}\text{O}_2/\text{CeO}_2\text{-SD}$ . It should be emphasized that for Au clusters on  $\text{CeO}_2\text{-SD}$ , we have explicitly added extra two O atoms into the system, which leads to oxidized Au clusters (the Au clusters with less than two extra O atoms are also studied as shown in the [supplementary material](#), which are less stable than those with two extra O atoms). In [Figs. 2\(a\)–2\(i\)](#), we illustrate the most stable structure identified from SSW-NN. The formation energy  $E_{\text{form}}^{\text{Au}}$  of these most stable Au clusters can be computed with respect to the bulk fcc Au metal, the gas phase  $\text{O}_2$ , and the clean surface, as shown in the following equation:

$$E_{\text{form}}^{\text{Au}} = \frac{E_{\text{slab}} - E_{\text{clean}} - N_{\text{Au}}E_{\text{Au}} - N_{\text{O}} \times 0.5 \times E_{\text{O}_2}}{N_{\text{Au}}} \quad (8)$$

In [Eq. \(8\)](#),  $E_{\text{slab}}$ ,  $E_{\text{Au}}$ , and  $E_{\text{clean}}$  are the total energy of the most stable structure, corresponding to bulk, Au, and clean surfaces ( $\text{CeO}_2\text{-p}$ ,  $\text{CeO}_2\text{-O}_v$ , or  $\text{CeO}_2\text{-SD}$ ).  $N_{\text{Au}}$  and  $N_{\text{O}}$  are the number of Au and O atoms in the Au cluster:  $N_{\text{O}}$  equals 2 for the oxidized clusters on  $\text{CeO}_2\text{-SD}$  and is zero in the other cases. The overall energetic profile for  $E_{\text{form}}^{\text{Au}}$  is plotted in [Fig. 2\(j\)](#).

As shown, the  $E_{\text{form}}^{\text{Au}}$  energetics of Au clusters on the pristine  $\text{CeO}_2$  drops gradually from +0.78 eV to +0.69 and to +0.64 eV (eV/Au atom). They are generally poorer compared to them on other two  $\text{CeO}_2$  surfaces, suggesting that the ultrasmall clusters do not prefer to anchor on the pristine surface, and the larger cluster is thermodynamically more favored. The presence of the O vacancy, interestingly, does not much increase the  $E_{\text{form}}^{\text{Au}}$  for the Au clusters (note that this small energy difference is above the NN error bar for the supported systems as shown in [Fig. S2](#) of the [supplementary material](#)). The similar energetics for Au on pristine  $\text{CeO}_2$  and  $\text{CeO}_2$  with O vacancy indicates that the O vacancy does not induce much additional charge transfer, e.g., from  $\text{CeO}_2$  support to Au in forming a negatively charged Au cluster. In fact, the additional electrons due to the missing of a surface O are stored in nearby surface Ce atoms, forming two  $\text{Ce}^{3+}$ . This explanation is supported by our DFT calculations that the net magnetic spin for  $\text{Au}_x/\text{CeO}_2\text{-O}_v$  systems is generally larger than 2, suggesting that the Au adsorption does not quench the spin on Ce atoms.

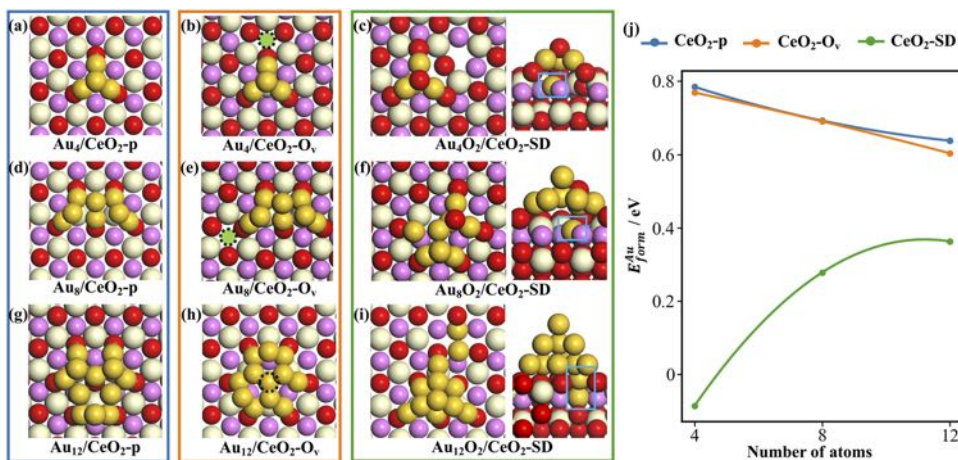


**FIG. 2.** Global minimum structures for various Au clusters on  $\text{CeO}_2$  determined by SSW-NN. [(a)–(i)] Structure snapshots of Au clusters on three different  $\text{CeO}_2$  surfaces. For  $\text{Au}_x\text{O}_2/\text{CeO}_2\text{-SD}$ , both the top and the side views are shown for clarity. Au atoms are in yellow, and also see the caption of [Fig. 1](#) for other atoms. The oxygen vacancy is indicated by dashed circles with/without the filled green color in  $\text{Au}_x/\text{CeO}_2\text{-O}_v$ . The embedded Au atom is highlighted by a blue rectangle. (j) The formation energy of the Au cluster as computed from [Eq. \(8\)](#).

On the other hand, the oxidized Au clusters on **CeO<sub>2</sub>-SD** are much stabilized as reflected by the lower  $E_{form}^{Au}$ . In particular, **Au<sub>4</sub>O<sub>2</sub>/CeO<sub>2</sub>-SD** has a negative formation energy,  $-0.085$  eV/Au atom, which suggests that the **CeO<sub>2</sub>-SD** can act as the anchoring site for ultrasmall oxidized Au clusters below 4 Au atoms. With the increase in the cluster size, the energetic preference at the **CeO<sub>2</sub>-SD** sites disappears gradually. In the following, we elaborate their atomic structures.

**Au<sub>x</sub>/CeO<sub>2</sub>-p**. Our results show that the ultrasmall Au clusters even with only four atoms exhibit a two-layer structure on pristine CeO<sub>2</sub>(111). For the **Au<sub>4</sub>/CeO<sub>2</sub>-p**, the most stable configuration is a Au<sub>4</sub> tetrahedron landing on three exposed surface O atoms. Three Au–O bonds between gold cluster and CeO<sub>2</sub> stabilize the cluster, and the Au–Ce distances are 3.90–3.93 Å for the bottom layer Au atoms. The Au<sub>8</sub> and Au<sub>12</sub> clusters have more Au–O bonds, five and six, respectively, and also exhibit 3-D packing structures. The other Au atoms grow nearby to glue the Au–O moieties together. We noted that with the increase in the cluster size, the PES of the Au cluster becomes flat. In particular, the Au<sub>12</sub>/CeO<sub>2</sub>-p has several energetically degenerate minima, less than 0.11 eV energy difference, and they differ only slightly in the positions of gluing Au atoms (see Fig. S2 of the [supplementary material](#) for detail).

**Au<sub>x</sub>/CeO<sub>2</sub>-O<sub>v</sub>**. The structures of Au<sub>x</sub> supported on **CeO<sub>2</sub>-O<sub>v</sub>** are, in general, similar to their counterpart on pristine CeO<sub>2</sub>. The Au clusters in the most stable configuration for **Au<sub>4</sub>/CeO<sub>2</sub>-O<sub>v</sub>** and **Au<sub>8</sub>/CeO<sub>2</sub>-O<sub>v</sub>** mimic the corresponding ones on **CeO<sub>2</sub>-p** since the O vacancy is at the subsurface and appears nearby the Au cluster. In particular, the Au–Ce distances are 3.64–4.07 Å for the bottom layer Au atoms in **Au<sub>4</sub>/CeO<sub>2</sub>-O<sub>v</sub>**. For the Au<sub>12</sub> cluster, the O vacancy is right beneath the Au clusters and at the surface layer. The Au<sub>12</sub> cluster already exhibits a close-packing crystal structure with the seven atoms in the bottom layer (six of them bonding with surface O) and five atoms in the top layer. It is noted that the similar close-packing pattern has also been reported previously via manual construction.<sup>61</sup>

**Au<sub>x</sub>O<sub>2</sub>/CeO<sub>2</sub>-SD**. The structures of Au<sub>x</sub>O<sub>2</sub> supported on **CeO<sub>2</sub>-SD** are quite different from the other systems without extra O atoms. For all three systems, we noticed that the missing Ce vacancy on the surface will always be filled by one Au atom, indicating that the embedded Au atom is positively charged to replace the missing Ce<sup>4+</sup> cation and the other Au<sub>x-1</sub> cluster then grows upon/nearby this embedded Au. The two extra O atoms tend to either cap a Au<sub>3</sub> cluster or to refill the lattice O position. The **Au<sub>4</sub>O<sub>2</sub>/CeO<sub>2</sub>-SD** has a Au<sub>3</sub>O tetrahedron on top of the embedded Au with the three Au bonding to three surface O atoms. The Au<sub>3</sub>O tetrahedron structure is quite similar to the Au<sub>4</sub> on pristine CeO<sub>2</sub>, except the distance between Au and surface O is now shorter (2.0 Å in **Au<sub>4</sub>O<sub>2</sub>/CeO<sub>2</sub>-SD** vs 2.05 Å in **Au<sub>4</sub>/CeO<sub>2</sub>-p**); the Au–Ce distances are 3.33–3.34 Å for the embedded Au and are ranging from 3.30 to 3.82 for the other three Au atoms. This very short Au–Ce contact agrees well with the previous EXAFS measurement by Tibiletti *et al.* (3.35 Å),<sup>18</sup> which is regarded as the evidence for cationic Au. The **Au<sub>8</sub>O<sub>2</sub>/CeO<sub>2</sub>-SD** is based on Au<sub>4</sub>O<sub>2</sub>/CeO<sub>2</sub>-SD with the growth of the other four Au atoms nearby the Au<sub>3</sub>O. For the **Au<sub>12</sub>O<sub>2</sub>/CeO<sub>2</sub>-SD**, the structure is dramatically different and can be regarded as a close-packing three-layer Au<sub>10</sub> cluster together with an embedded Au<sub>2</sub> cluster. The Au<sub>10</sub> cluster has six, three, and one Au atoms in the first, second, and third layers, respectively. The formation of the large close-packing

Au clusters indicates the diminishing energetic preference at the **CeO<sub>2</sub>-SD** site.

## B. Segregation and diffusion of Au clusters

Having determined the stable configuration of Au clusters, we are now at the position to answer the aggregation/segregation ability of Au clusters on CeO<sub>2</sub>. Considering that the pristine surface is the dominant structural pattern so that the aggregation/segregation will inevitably involve the migration on the pristine surface, we, therefore, focus on the diffusion of Au clusters on pristine CeO<sub>2</sub>(111). To this goal, we have selected the **Au<sub>8</sub>/CeO<sub>2</sub>-p** as the model system and utilized the enhanced MD technique to follow the possible kinetics events by gradually reducing the Au coordination as defined by the general coordinate  $\xi$  in Sec. II. This is done by adding consecutively bias potential  $\xi$ , which comprises the pair distance between Au atoms to reflect the Au coordination [see Eqs. (1)–(4)].

In our simulation, a series of biased MD simulations centering at a different general reaction coordination  $\xi_m$  window were performed starting from the **Au<sub>8</sub>/CeO<sub>2</sub>-p** global minimum. The  $\xi_m$  decreases with the increase in  $m$ . The simulation was terminated until the decomposition of the Au<sub>8</sub> cluster into smaller clusters occurs, which takes  $\sim 450$  windows. Then, the snapshots along MD trajectories were quenched to zero temperature by local optimization to identify the intrinsic structures that associate with the finite-temperature MD trajectory. Finally, the reaction pathways between two consecutive structures were connected and the transition state (TS) was located by using the double-ended surface walking (DESW) method<sup>62</sup> (more details on the DESW method can be found in the [supplementary material](#)).

Figure 3 shows the reaction energy profile and the reaction snapshots for the **Au<sub>8</sub>/CeO<sub>2</sub>-p** (state **A**) segregation pathway into two neighboring **Au<sub>4</sub>/CeO<sub>2</sub>-p** (state **G**) via five intermediates, namely, **B** to **F** states. The TS structures for **A** → **B**, being **TS1** state, and **B** → **C** transition, being **TS2** state, are also highlighted. It can be found that the elementary step between two consecutive intermediates involves an Au–O bond forming or breaking, except for **E** → **F** transition where the Au<sub>8</sub> cluster finally breaks into two Au<sub>4</sub> fragments.

We may have a close look on how the atom moves in the segregation process. The initial steps, including **A** → **B** and **B** → **C**, are highly activated, which has a reaction barrier of 1.60 eV. In these steps, the top layer atoms in the cluster, i.e., the atoms **1**, **2**, and **4** as labeled in Fig. 3, move apart to reduce their coordination, namely, the *spreading stage*. Specifically, the Au atom **4** moves down to the first layer and the atoms **1** and **2** shift away from the center of mass. Together with these top layer atoms' movement, the bottom layer Au atom **3** moves up to refill the gap due to the splitting of top layer atoms. Overall, from **A** to **C**, the cluster spreads out to occupy more surface atoms of CeO<sub>2</sub> with the average Au coordination decreasing from 2.72 to 2.25, and in the meantime, the number of Au–O bonds decrease from 5 to 4.

After the state **C**, the cluster continues to deform to find the better configuration, namely, the *reclustering stage*. The first Au<sub>4</sub> tetrahedron appears in the state **E**, and the transition from **C** to **E** decreases in energy. The transition in **C** → **D** is straightforward, where the Au atom **5** moves up and forms a straight line with the other three Au atoms at the top layer. From **D** to **E**, the Au atoms **1**

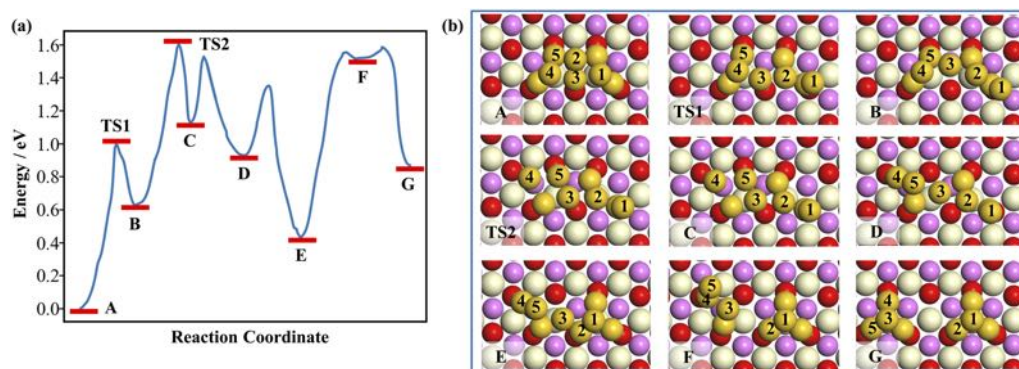


**FIG. 3.** Reaction energy profile (a) and key structure snapshots (b) for the  $\text{Au}_8$  cluster segregation on  $\text{CeO}_2\text{-p}$ . **A** is the global minimum structure of the  $\text{Au}_8$  cluster on  $\text{CeO}_2\text{-p}$ , and its energy is set as zero. The minimum energy pathway is obtained by extrapolating the transition state (TS) using a steep descendent local optimization technique toward two neighboring minima. (b) Key Au atoms are labeled by numbers. In addition, see Fig. 2 caption for the color scheme of atoms.

and 2 at the right corner reform to generate the stable  $\text{Au}_4$  tetrahedron, where atom 2 finally moves to the bottom layer to bond with surface O. Compared to initial state **A**, one can see that two pairs of Au atoms swap their layer positions, 4–5 pair and 2–3 pair, which suggests that the segregation pathway requires a large structural deformation of the cluster: at the *spreading stage*, the top layer atoms move downwards to bond with the oxide support, while at the *reclustering stage*, the bottom layer atoms move upwards to restore the local high coordination.

The segregation process is complete until the second  $\text{Au}_4$  tetrahedron forms from **E** to **G**. The reaction is again highly activated with the barrier 1.23 eV due to the presence of a high energy metastable state **F**, where the linkage Au atom 3 breaks completely from the nascent  $\text{Au}_4$  tetrahedron. The four Au atoms in state **F** can rearrange facily to become a second  $\text{Au}_4$  tetrahedron in state **G**.

It should be mentioned that once the  $\text{Au}_4$  cluster forms on the pristine surface, it can migrate with a slightly lower barrier (1.38 eV) than the  $\text{Au}_8$  cluster segregation. The lowest energy pathway for the  $\text{Au}_4$  migration is shown in Fig. 4. The diffusion of the  $\text{Au}_4$  can also be divided into two individual stages, namely, the *spreading* and the *reclustering*. As shown, the highest energy metastable state ( $\beta$ ) has a low Au–Au coordination, where the cluster has a planar geometry with all four atoms lying on the surface.

The high barrier of Au cluster segregation (1.60 eV) on the pristine surface implies that the sintering of small Au clusters might occur only locally between neighboring small Au clusters at low temperatures (e.g., <500 K). Once the Au cluster reaches to a certain size, e.g., above 8 atoms, the segregation and diffusion become difficult kinetically. Our finding is consistent with the observed high stability of Au clusters for WGS on Au/ $\text{CeO}_2$  catalysts by Kim and Thompson, who showed that the sintering was slow and the deactivation was mainly due to surface fouling by carbonate species.<sup>63</sup>

Overall, we found that both the segregation and diffusion of Au clusters on pristine  $\text{CeO}_2$  require a high activation energy. From our results, the most stable Au clusters on  $\text{CeO}_2\text{-p}$ , even with only

four atoms, are in 3-dimensional closed-packed morphology. Both the segregation and migration thus need to deform the Au cluster significantly, where a number of Au–Au bonds break in the process. Apparently, the high barrier is related to the corrugated PES for Au cluster deformation on the  $\text{CeO}_2$  surface. It is, therefore, important to understand what controls the PES of the Au cluster on  $\text{CeO}_2$ . The answer of this would help us to reveal our observations, for example, 3-dimensional closed-packed  $\text{Au}_x$  clusters ( $x < 12$ ) are preferred on the  $\text{CeO}_2$  surface, but their counterparts in the gas phase adopt planar structures.

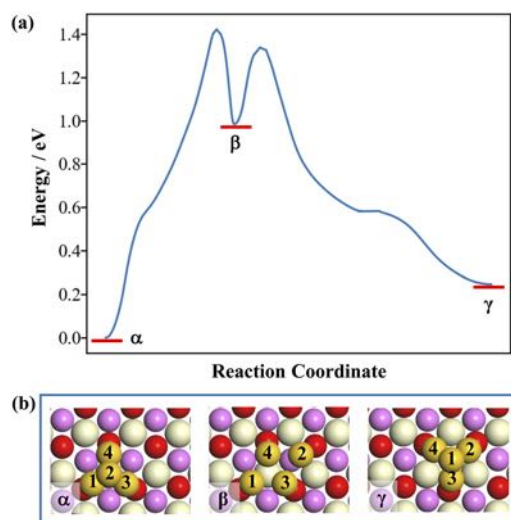


**FIG. 4.** Reaction energy profile (a) and key snapshots (b) for the  $\text{Au}_4$  cluster diffusion  $\text{CeO}_2\text{-p}$ .  $\alpha$  is the global minimum structure of  $\text{Au}_4$  cluster on  $\text{CeO}_2\text{-p}$ , and its energy is set as zero. The minimum energy pathway is obtained by extrapolating the transition state (TS) using a steep descendent local optimization technique toward two neighboring minima. In addition, see Fig. 2 caption for the color scheme of atoms.

### C. Electronic structure analysis of Au<sub>4</sub> on CeO<sub>2</sub>-p

We thus go further to compare the electronic structures for two different Au<sub>4</sub> clusters on CeO<sub>2</sub>-p, i.e., the tetrahedron Au<sub>4</sub>/CeO<sub>2</sub>-p and the planar Au<sub>4</sub>/CeO<sub>2</sub>-p, from the pathway of Au<sub>4</sub> diffusion on CeO<sub>2</sub>-p. A large energy gap, 0.98 eV, is present between the two states, which is the key reason that Au cluster diffusion on the CeO<sub>2</sub> is highly activated. DFT calculations have been performed to converge the wavefunction of the two large systems, which show that both systems are spin-polarized: the net spin is 1.0 for tetrahedron Au<sub>4</sub>/CeO<sub>2</sub>-p and 0.82 for planar Au<sub>4</sub>/CeO<sub>2</sub>-p. This is quite interesting considering that the CeO<sub>2</sub>-p surface is stoichiometric and the appearance of spin polarization has to arise from the charge transfer between Au and CeO<sub>2</sub>. We, therefore, plotted the spin density for the two systems in order to identify where the spin state is localized.

Figure 5 shows that the spin electron for both systems has a *f*-orbital shape and is localized on the central Ce atom that is directly beneath the Au cluster. There is no significant difference in the spin density map between the tetrahedron and planar Au<sub>4</sub>/CeO<sub>2</sub>-p. It should be mentioned that the electron transfer from a single adsorbed Au atom to surface Ce as mediated by the surface O has been revealed since the work of Liu.<sup>25,64</sup> Here, we emphasize that this important phenomenon, namely, the Au-to-Ce electron transfer, remains with the increase in the Au cluster size. It is interesting that only one Ce atom is reduced even if the cluster has four Au atoms and bonds with three surface O anions.

Overall, according to the spin analysis, one can conclude that a surface Ce upon Au<sub>4</sub> adsorption is reduced from Ce<sup>4+</sup> to Ce<sup>3+</sup>, and consequently, the Au<sub>4</sub> cluster is positively charged as Au<sub>4</sub><sup>+</sup>. The diffusion of the Au cluster on CeO<sub>2</sub> is, therefore, governed by the PES of positively charged Au cluster on CeO<sub>2</sub>. For comparison, we, therefore, first examined the gas phase tetrahedron Au<sub>4</sub> (T<sub>4</sub> symmetry) and planar Au<sub>4</sub> (C<sub>s</sub> symmetry) with and without the positive charge using DFT calculations. We found that in the charge-neutral case, the planar Au is strongly preferred over the tetrahedron Au<sub>4</sub> by 1.05 eV per cluster. This energy preference is much reduced to 0.42 eV per cluster when the cluster is positively charged. Obviously, the energy preference for the gas phase Au cluster is totally

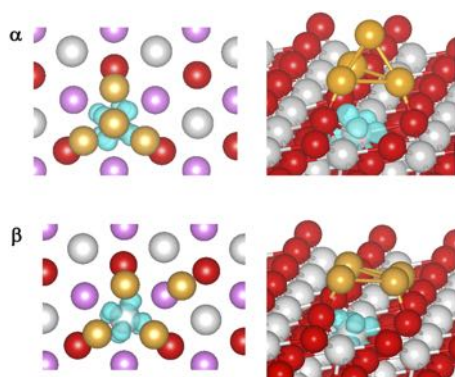


**FIG. 5.** Spin charge density (blue) contour plot for two different Au<sub>4</sub> conformations ( $\alpha$ : tetrahedron and  $\beta$ : plane) on CeO<sub>2</sub>-p, including both the top (left) and side (right) views. In addition, see Fig. 2 caption for the color scheme of atoms.

different from that in Au<sub>4</sub>/CeO<sub>2</sub>-p, where the tetrahedron structure is reversely much favored than the planar structure (by 0.98 eV). This suggests that the presence of Au–O bonding in the Au/CeO<sub>2</sub> system leads to the tetrahedron Au<sub>4</sub> structure, where the top layer Au atom acts as the capping group to fulfill the linear O–Au–Au bonding pattern of the bottom layer Au. The same can also be utilized to rationalize the global minimum structure of Au<sub>4</sub>O<sub>2</sub>/CeO<sub>2</sub>-SD, where one O atom acts as the capping group to terminate the planar Au<sub>3</sub> cluster (Fig. 2).

### IV. GENERAL DISCUSSIONS

Now, we are at the position to discuss the chemistry of Au growth on CeO<sub>2</sub>. Our results show that the ultrasmall Au clusters on both the pristine surface and surface with O vacancy are unstable with respect to the bulk Au metal as reflected by positive  $E_{form}^{Au}$ . With the increase in the cluster size, the formation energy gradually drops (Fig. 2), indicating that the Au cluster aggregation is thermodynamically favored. Since the pristine sites should dominate the surface area of CeO<sub>2</sub> support, the growth of crystalline Au nanoparticles for dispersed Au clusters on pristine and O-vacancy sites is thermodynamically inevitable in catalyst synthesis.

Importantly, we find that an ultrasmall ionic Au cluster, e.g., less than four atoms, can attach strongly to the surface structural defects with a negative  $E_{form}^{Au}$ . It, thus, suggests that once such defected surface sites are available, they can anchor ultrasmall cationic Au clusters that are resistant to sintering in catalyst preparation (our high temperature MD simulations also confirm the high stability as detailed in Sec. 3 of the [supplementary material](#)). Experimentally, these structural defects on oxide can indeed be created by synthesizing nanosized CeO<sub>2</sub> particles,<sup>44,65</sup> where the apex, edges, and boundaries are the common structural defects. For example, Fu *et al.* have utilized 10% La doping to achieve ~5 nm sized CeO<sub>2</sub> particles, where the addition of La was known to reduce CeO<sub>2</sub> particle size and prevent sintering of Au.<sup>13,66</sup>

In addition to the benefit of CeO<sub>2</sub> structural defects to anchor cationic Au, from our kinetics results of Au cluster segregation/diffusion, we found that another merit of CeO<sub>2</sub> is that the Au cluster diffusion on CeO<sub>2</sub> is highly activated due to the corrugated PES of the Au cluster. This would help us to reduce the particle size of Au and thus facilitate the catalytic reactions on Au that generally involve the low-coordinated sites (e.g., CO adsorption).<sup>67,68</sup>

The corrugated PES of the Au cluster on CeO<sub>2</sub> is related to both the Au–O (CeO<sub>2</sub>) bonding and the Au–Au bonding. An obvious observation for the consequence of Au–CeO<sub>2</sub> interaction is, as also noticed by other groups, the early 2-D to 3-D transformation of the Au cluster (e.g., Au<sub>4</sub>) on CeO<sub>2</sub>,<sup>29,61,69,70</sup> considering that the unsupported (free) Au clusters prefer the 2-dimensional (2-D) planar structure until Au<sub>12</sub> ~ Au<sub>13</sub>.<sup>71</sup> This strong preference of 3D structure for the supported Au cluster has been attributed to the Au cluster interaction with CeO<sub>2</sub> surface on two aspects: (i) The presence of CeO<sub>2</sub>, in particular, the presence of Au–O bonding at the interface, alters the Au–Au bond strength and thus changes the Au cluster potential energy surface.<sup>29,69</sup> Previous studies have found that the early transition metal (TM) atoms (e.g., Ru, Rh, Os, and Ir) tend to form a stronger TM–O bond and thus favor the 2-D configuration; instead, the late TM atoms (e.g., Pt and Au) prefer the 3-D configuration due to stronger TM–TM bonds.<sup>69</sup> (ii) The unique



charge transfer from the Au cluster to CeO<sub>2</sub> support can partially reduce surface Ce<sup>4+</sup> to Ce<sup>3+</sup> ions and produce a positively charged Au cluster.<sup>69,70</sup> This positive charge on the Au cluster would enhance the electron localization in the d-states of Au and thus reduce the d-states hybridization, which is repulsive in nature due to the full d-shell of Au. According to previous hybrid-DFT<sup>72</sup> (Rh<sub>n</sub>, n = 2–15) and DFT + U<sup>73</sup> (Co<sub>13</sub>) calculations, an enhancement of the late transition metal Rh and Co d-states localization increases the stability of compact 3-D structures relative to the planar 2-D structures. Following this line, Kim *et al.*<sup>29</sup> also postulated that the charge transfer would break the balance of s-d hybridization and thus drive the structural evolution from 2-D to 3-D for the Au cluster on CeO<sub>2</sub> support.

Finally, we must also add a few more words to distinguish the two stages in Au/CeO<sub>2</sub> catalysis, namely, the catalyst preparation and the catalytic reaction, which may have very different reductive conditions. The Au/CeO<sub>2</sub> catalyst is synthesized generally in air under ambient conditions.<sup>13,63</sup> From our results, the presence of cationic Au, e.g., Au<sub>4</sub>O<sub>2</sub>/CeO<sub>2</sub>-SD, is allowed in the thermodynamics equilibrium with the gas phase O<sub>2</sub>. By contrast, the CO reactant and H<sub>2</sub> product in the WGS reaction are both highly reductive molecules, and thus, under the reaction conditions, the cationic Au are thermodynamically unstable and will be reduced to metallic Au. By distinguishing these two different chemical environments, we can, therefore, reconcile the observations from experiment and previous calculations.

For example, Zhang *et al.* have analyzed the thermodynamics of the Au adatom under the WGS reaction condition and found that the cationic Au is not stable compared to Au at the O vacancy.<sup>74</sup> The cationic Au reduction to metallic Au was also observed in experiment by Tibiletti *et al.* using *in situ* X-ray adsorption spectra,<sup>18</sup> and they suggested that small metallic Au is the active site under WGS reaction conditions. However, in the studies by Fu *et al.*<sup>13</sup> and Guzman *et al.*,<sup>17</sup> the cationic Au are characterized as the key reaction site based on the knowledge about the freshly prepared catalyst. Although Au clusters supported on CeO<sub>2</sub> will naturally donate electrons to Ce to become positively charged Au clusters, we emphasize that the cationic Au clusters do have clear indications in experiment, e.g., the short Au–Ce contact (3.35 Å) and the characteristic Au–CO IR frequency. From our results, the extra O atoms in the ultrasmall Au cluster is the key to produce the cationic Au cluster and the embedded Au atoms do have the Au–Ce short contact as observed in experiment.

## V. CONCLUDING REMARKS

This work represents the latest theoretical effort toward elucidating the active site structure of the Au/CeO<sub>2</sub> catalyst. With the advent of the SSW-NN method to combine machine learning and global optimization techniques, it is now feasible to simulate directly nanosized metal clusters on oxide support at a low computational cost but with the accuracy close to first principles calculations. As our first application, this work generates the ternary Au–Ce–O G-NN potential and searches the PES for ultrasmall metal clusters on oxide, which is relevant to Au/CeO<sub>2</sub> catalysis. The segregation and diffusion pathways are also examined by using enhanced MD to understand the kinetics stability of ultrasmall Au clusters. Our major conclusions are outlined as follows:

- (i) By training 33 654 first principles global dataset, the ternary Au–Ce–O G-NN potential achieves a rms accuracy of 6.115 meV/atom in energy and 0.152 eV/Å in force. The G-NN can be utilized for global optimization and enhanced MD simulation of Au clusters on different CeO<sub>2</sub> surfaces.
- (ii) The geometry of supported Au clusters is sensitive to both the size of cluster and the structure of support and is totally different from their gas phase counterparts. The SSW-NN provides a convenient solution to identify the global minimum of supported Au clusters. In general, ultrasmall Au clusters on CeO<sub>2</sub> prefer a three-dimensional close-packing structure, which is due to the strong interaction between Au and CeO<sub>2</sub>. Electron transfer occurs generally between the Au cluster and neighboring Ce that reduces Ce<sup>4+</sup> to Ce<sup>3+</sup>.
- (iii) Except for Au<sub>4</sub>O<sub>2</sub> cluster anchoring at the CeO<sub>2</sub> structural defects, all the other clusters investigated, including Au<sub>4</sub>, Au<sub>8</sub>, and Au<sub>12</sub> on pristine CeO<sub>2</sub> and CeO<sub>2</sub> with O vacancy, Au<sub>8</sub>O<sub>2</sub> and Au<sub>12</sub>O<sub>2</sub> on CeO<sub>2</sub> with structural defects, are all thermodynamically unstable and thus prefer sintering into large Au particles. The ultrasmall Au cationic clusters (e.g., Au<sub>4</sub>O<sub>2</sub>) anchoring at the CeO<sub>2</sub> structural defects can survive in catalyst preparation and they are expected to, after transforming to metallic Au cluster, act as the active site for catalytic reactions.
- (iv) The Au clusters on pristine CeO<sub>2</sub> are kinetically stable. The segregation barrier for a Au<sub>8</sub> cluster on CeO<sub>2</sub> is 1.60 eV, which produces two Au<sub>4</sub> clusters. The diffusion barrier for a Au<sub>4</sub> cluster is 1.38 eV. The high barrier supports the fact that CeO<sub>2</sub> is a good support material to disperse small Au clusters.

## SUPPLEMENTARY MATERIAL

See the [supplementary material](#) for Au–Ce–O global NN potential construction, description of double-ended surface walking method, the formation energy of supported Au clusters with less than two extra O atoms, low-lying structures for Au<sub>12</sub>/CeO<sub>2</sub>-p, high temperature MD trajectory for Au<sub>4</sub>O<sub>2</sub>/CeO<sub>2</sub>-SD, and XYZ coordination for all supported Au clusters on ceria in [Fig. 2](#).

## ACKNOWLEDGMENTS

This work was supported by the National Key Research and Development Program of China (Grant No. 2018YFA0208600) and the National Science Foundation of China (Grant Nos. 21573149, 21533001, and 91745201).

The authors declare no competing financial interests.

## REFERENCES

- <sup>1</sup>M. Haruta, *Nature* **437**(7062), 1098–1099 (2005).
- <sup>2</sup>A. S. K. Hashmi and G. J. Hutchings, *Angew. Chem., Int. Ed.* **45**(47), 7896–7936 (2006).
- <sup>3</sup>M. Haruta, N. Yamada, T. Kobayashi, and S. Iijima, *J. Catal.* **115**(2), 301–309 (1989).
- <sup>4</sup>B. Qiao, J.-X. Liang, A. Wang, C.-Q. Xu, J. Li, T. Zhang, and J. J. Liu, *Nano Res.* **8**(9), 2913–2924 (2015).
- <sup>5</sup>A. Wittstock, V. Zielasek, J. Biener, C. M. Friend, and M. Bäumer, *Science* **327**(5963), 319 (2010).

- <sup>6</sup>M. Kantcheva, O. Samarskaya, L. Ilieva, G. Pantaleo, A. M. Venezia, and D. Andreeva, *Appl. Catal., B* **88**(1), 113–126 (2009).
- <sup>7</sup>L. Ilieva, G. Pantaleo, N. Velinov, T. Tabakova, P. Petrova, I. Ivanov, G. Avdeev, D. Paneva, and A. M. Venezia, *Appl. Catal., B* **174–175**, 176–184 (2015).
- <sup>8</sup>J. Guzman and B. C. Gates, *Angew. Chem., Int. Ed.* **42**(6), 690–693 (2003).
- <sup>9</sup>H. Häkkinen, S. Abbet, A. Sanchez, U. Heiz, and U. Landman, *Angew. Chem., Int. Ed.* **42**(11), 1297–1300 (2003).
- <sup>10</sup>J. A. Rodriguez, P. Liu, J. Hrbek, J. Evans, and M. Pérez, *Angew. Chem., Int. Ed.* **46**(8), 1329–1332 (2007).
- <sup>11</sup>M. Stratakis and H. Garcia, *Chem. Rev.* **112**(8), 4469–4506 (2012).
- <sup>12</sup>J. A. Rodriguez, *Catal. Today* **160**(1), 3–10 (2011).
- <sup>13</sup>Q. Fu, H. Saltsburg, and M. Flytzani-Stephanopoulos, *Science* **301**(5635), 935 (2003).
- <sup>14</sup>H. Sakurai, T. Akita, S. Tsubota, M. Kiuchi, and M. Haruta, *Appl. Catal., A* **291**(1), 179–187 (2005).
- <sup>15</sup>N. J. Lawrence, J. R. Brewer, L. Wang, T.-S. Wu, J. Wells-Kingsbury, M. M. Ihrig, G. Wang, Y.-L. Soo, W.-N. Mei, and C. L. Cheung, *Nano Lett.* **11**(7), 2666–2671 (2011).
- <sup>16</sup>D. Widmann, R. Leppelt, and R. J. Behm, *J. Catal.* **251**(2), 437–442 (2007).
- <sup>17</sup>J. Guzman, S. Carrettin, and A. Corma, *J. Am. Chem. Soc.* **127**(10), 3286–3287 (2005).
- <sup>18</sup>D. Tibiletti, A. A. Fonseca, R. Burch, Y. Chen, J. M. Fisher, A. Goguet, C. Hardacre, P. Hu, and D. Thompsett, *J. Phys. Chem. B* **109**(47), 22553–22559 (2005).
- <sup>19</sup>C. H. Kim and L. T. Thompson, *J. Catal.* **244**(2), 248–250 (2006).
- <sup>20</sup>X. Wang, J. A. Rodriguez, J. C. Hanson, M. Pérez, and J. Evans, *J. Chem. Phys.* **123**(22), 221101 (2005).
- <sup>21</sup>J.-F. Jerratsch, X. Shao, N. Nilius, H.-J. Freund, C. Popa, M. V. Ganduglia-Pirovano, A. M. Burrow, and J. Sauer, *Phys. Rev. Lett.* **106**(24), 246801 (2011).
- <sup>22</sup>K. Košmider, V. Brázdová, M. V. Ganduglia-Pirovano, and R. Pérez, *J. Phys. Chem. C* **120**(2), 927–933 (2016).
- <sup>23</sup>D. A. Andersson, S. I. Simak, B. Johansson, I. A. Abrikosov, and N. V. Skorodumova, *Phys. Rev. B* **75**(3), 035109 (2007).
- <sup>24</sup>S. Fabris, G. Vicario, G. Balducci, S. de Gironcoli, and S. Baroni, *J. Phys. Chem. B* **109**(48), 22860–22867 (2005).
- <sup>25</sup>Z.-P. Liu, S. J. Jenkins, and D. A. King, *Phys. Rev. Lett.* **94**(19), 196102 (2005).
- <sup>26</sup>C. Zhang, A. Michaelides, D. A. King, and S. J. Jenkins, *J. Chem. Phys.* **129**(19), 194708 (2008).
- <sup>27</sup>M. F. Camellone and S. Fabris, *J. Am. Chem. Soc.* **131**(30), 10473–10483 (2009).
- <sup>28</sup>W. Song and E. J. M. Hensen, *ACS Catal.* **4**(6), 1885–1892 (2014).
- <sup>29</sup>H. Y. Kim, H. M. Lee, and G. Henkelman, *J. Am. Chem. Soc.* **134**(3), 1560–1570 (2012).
- <sup>30</sup>Y. Chen, J. Cheng, P. Hu, and H. Wang, *Surf. Sci.* **602**(17), 2828–2834 (2008).
- <sup>31</sup>C. Shang and Z.-P. Liu, *J. Chem. Theory Comput.* **9**(3), 1838–1845 (2013).
- <sup>32</sup>C. Shang, X.-J. Zhang, and Z.-P. Liu, *Phys. Chem. Chem. Phys.* **16**(33), 17845–17856 (2014).
- <sup>33</sup>S.-D. Huang, C. Shang, X.-J. Zhang, and Z.-P. Liu, *Chem. Sci.* **8**(9), 6327–6337 (2017).
- <sup>34</sup>S.-D. Huang, C. Shang, P.-L. Kang, and Z.-P. Liu, *Chem. Sci.* **9**(46), 8644–8655 (2018).
- <sup>35</sup>S. Ma, S.-D. Huang, and Z.-P. Liu, *Nat. Catal.* **2**(8), 671–677 (2019).
- <sup>36</sup>S. Ma, S.-D. Huang, Y.-H. Fang, and Z.-P. Liu, *ACS Catal.* **8**(10), 9711–9721 (2018).
- <sup>37</sup>A. Barducci, M. Bonomi, and M. Parrinello, *Wiley Interdiscip. Rev.: Comput. Mol. Sci.* **1**(5), 826–843 (2011).
- <sup>38</sup>J. Kästner, *Wiley Interdiscip. Rev.: Comput. Mol. Sci.* **1**(6), 932–942 (2011).
- <sup>39</sup>S.-D. Huang, C. Shang, P.-L. Kang, X.-J. Zhang, and Z.-P. Liu, *Wiley Interdiscip. Rev.: Comput. Mol. Sci.* **9**, e1415 (2019).
- <sup>40</sup>G. Kresse and J. Furthmüller, *Comput. Mater. Sci.* **6**(1), 15–50 (1996).
- <sup>41</sup>S. Ma, C. Shang, and Z.-P. Liu, *J. Chem. Phys.* **151**(5), 050901 (2019).
- <sup>42</sup>J. P. Perdew, K. Burke, and M. Ernzerhof, *Phys. Rev. Lett.* **77**(18), 3865–3868 (1996).
- <sup>43</sup>V. I. Anisimov, J. Zaanen, and O. K. Andersen, *Phys. Rev. B* **44**(3), 943–954 (1991).
- <sup>44</sup>F. Esch, S. Fabris, L. Zhou, T. Montini, C. Africh, P. Fornasiero, G. Comelli, and R. Rosei, *Science* **309**(5735), 752 (2005).
- <sup>45</sup>M. Nolan, S. C. Parker, and G. W. Watson, *J. Phys. Chem. B* **110**(5), 2256–2262 (2006).
- <sup>46</sup>N. C. Hernández, R. Grau-Crespo, N. H. de Leeuw, and J. F. Sanz, *Phys. Chem. Chem. Phys.* **11**(26), 5246–5252 (2009).
- <sup>47</sup>M. Nolan, S. C. Parker, and G. W. Watson, *Surf. Sci.* **595**(1), 223–232 (2005).
- <sup>48</sup>B. Herschend, M. Baudin, and K. Hermansson, *J. Chem. Phys.* **126**(23), 234706 (2007).
- <sup>49</sup>M. V. Ganduglia-Pirovano, J. L. F. Da Silva, and J. Sauer, *Phys. Rev. Lett.* **102**(2), 026101 (2009).
- <sup>50</sup>P. R. L. Keating, D. O. Scanlon, and G. W. Watson, *J. Phys.: Condens. Matter* **21**(40), 405502 (2009).
- <sup>51</sup>H.-Y. Li, H.-F. Wang, X.-Q. Gong, Y.-L. Guo, Y. Guo, G. Lu, and P. Hu, *Phys. Rev. B* **79**(19), 193401 (2009).
- <sup>52</sup>M. Nolan, S. Grigoleit, D. C. Sayle, S. C. Parker, and G. W. Watson, *Surf. Sci.* **576**(1), 217–229 (2005).
- <sup>53</sup>Y. Chen, P. Hu, M.-H. Lee, and H. Wang, *Surf. Sci.* **602**(10), 1736–1741 (2008).
- <sup>54</sup>C. Zhang, A. Michaelides, D. A. King, and S. J. Jenkins, *Phys. Rev. B* **79**(7), 075433 (2009).
- <sup>55</sup>G. Kresse and D. Joubert, *Phys. Rev. B* **59**(3), 1758–1775 (1999).
- <sup>56</sup>H. J. Monkhorst and J. D. Pack, *Phys. Rev. B* **13**(12), 5188–5192 (1976).
- <sup>57</sup>G. M. Torrie and J. P. Valleau, *J. Chem. Phys.* **66**(4), 1402–1408 (1977).
- <sup>58</sup>H.-Y. Li, H.-F. Wang, Y.-L. Guo, G.-Z. Lu, and P. Hu, *Chem. Commun.* **47**(21), 6105–6107 (2011).
- <sup>59</sup>S. Torbrügge, M. Reichling, A. Ishiyama, S. Morita, and Ó. Custance, *Phys. Rev. Lett.* **99**(5), 056101 (2007).
- <sup>60</sup>K. Reuter and M. Scheffler, *Phys. Rev. B* **65**(3), 035406 (2001).
- <sup>61</sup>C. Zhang, A. Michaelides, D. A. King, and S. J. Jenkins, *J. Am. Chem. Soc.* **132**(7), 2175–2182 (2010).
- <sup>62</sup>X.-J. Zhang, C. Shang, and Z.-P. Liu, *J. Chem. Theory Comput.* **9**(12), 5745–5753 (2013).
- <sup>63</sup>C. H. Kim and L. T. Thompson, *J. Catal.* **230**(1), 66–74 (2005).
- <sup>64</sup>C. Zhang, A. Michaelides, and S. J. Jenkins, *Phys. Chem. Chem. Phys.* **13**(1), 22–33 (2011).
- <sup>65</sup>C. T. Campbell and C. H. F. Peden, *Science* **309**(5735), 713 (2005).
- <sup>66</sup>M. Flytzani-Stephanopoulos, *Acc. Chem. Res.* **47**(3), 783–792 (2014).
- <sup>67</sup>D. C. Meier and D. W. Goodman, *J. Am. Chem. Soc.* **126**(6), 1892–1899 (2004).
- <sup>68</sup>Z.-P. Liu, P. Hu, and A. Alavi, *J. Am. Chem. Soc.* **124**(49), 14770–14779 (2002).
- <sup>69</sup>M. J. Piotrowski, P. Tereshchuk, and J. L. F. Da Silva, *J. Phys. Chem. C* **118**(37), 21438–21446 (2014).
- <sup>70</sup>P. Tereshchuk, R. L. H. Freire, C. G. Ungureanu, Y. Seminovski, A. Kiejna, and J. L. F. Da Silva, *Phys. Chem. Chem. Phys.* **17**(20), 13520–13530 (2015).
- <sup>71</sup>D. J. Wales and J. P. K. Doye, *J. Phys. Chem. A* **101**(28), 5111–5116 (1997).
- <sup>72</sup>J. L. F. Da Silva, M. J. Piotrowski, and F. Aguilera-Granja, *Phys. Rev. B* **86**(12), 125430 (2012).
- <sup>73</sup>M. J. Piotrowski, P. Piquini, L. Cândido, and J. L. F. Da Silva, *Phys. Chem. Chem. Phys.* **13**(38), 17242–17248 (2011).
- <sup>74</sup>C. Zhang, A. Michaelides, D. A. King, and S. J. Jenkins, *J. Phys. Chem. C* **113**(16), 6411–6417 (2009).